

Robustness of embedded topological modes in bulk-like GeTe-Sb₂Te₃ heterostructures

Hisao Nakamura^{1,2*}, Johannes Hofmann^{3,4*}, Nobuki Inoue⁵, Sebastian Koelling⁶, Paul M. Koenraad⁶, Gregor Mussler⁷, Detlev Grtzmacher⁷, and Vijay Narayan^{8*}

¹ CD-FMat, National Institute of Advanced Industrial Science and Technology (AIST), 1-1-1 Umezono, Tsukuba Central 2, Tsukuba, Japan

² Department of Materials Science and Metallurgy, University of Cambridge, 27 Charles Babbage Road, Cambridge CB3 0FS, United Kingdom

³ Department of Applied Mathematics and Theoretical Physics, University of Cambridge, Centre for Mathematical Sciences, Cambridge CB3 0WA, United Kingdom

⁴ TCM Group, Cavendish Laboratory, University of Cambridge, Cambridge CB3 0HE, United Kingdom

⁵ RIKEN Center for Computational Science, 7-1-26 Minatojima-minami, Cyuo-ku, Kobe, Hyogo 650-0047, Japan

⁶ Eindhoven University of Technology, 5600 MB Eindhoven, The Netherlands

⁷ Peter Grnberg Institute (PGI-9), Forschungszentrum Jlich, 52425 Jlich, Germany

⁸ Department of Physics, University of Cambridge, J. J. Thomson Avenue, Cambridge CB3 0HE

E-mail: h.namura@gmail.com, jbh38@cam.ac.uk, vn237@cam.ac.uk

Abstract. The interface between a topological insulator and a normal insulator hosts localized states that appear due to the change in band structure topology. While these states are topologically protected, states at separate interfaces can hybridize and gap out. An important question is whether there are other factors, such as local fields and/or disorder, that may also impact these states. In this paper, we use a combination of experiment and theory to study heterostructures of GeTe (normal insulator) and Sb₂Te₃ (topological insulator) in which, due to the strong chemical affinity between the materials, there is significant intermixing at the interface where the topological state is expected. To characterize the interface, we evaluate the band offset between GeTe and Sb₂Te₃ using X-ray photoemission spectroscopy and use atom probe tomography to chart the elemental composition along the stacking direction. We then use first-principles calculations to independently calculate the band offset value and also to parametrize the band structure within a four-band continuum framework. Strikingly, the continuum model reveals that the interfacial topological modes can couple over significantly longer distances when the normal insulator medium is intermixed GeTe and Sb₂Te₃ rather than simply GeTe. We confirm this finding using first-principles calculation for thin heterostructure, which indicate that a disordered interface is sufficient to induce long-range coupling between embedded topological modes. Our study provides insights into how to use bulk-like structures to manipulate topological modes. Our results also provide a microscopic basis for recent experimental findings [Nguyen *et al.*, *Sci. Rep.* **6**, 27716 (2016)] where topological interface states were seen to couple over relatively large distances.

Submitted to: *New J. Phys.*

1. INTRODUCTION

The Ge-Sb-Te (GST) system has been widely studied due to its multi-functional character including phase-change properties [1–6], ferroelectric characteristics [7,8], and potential thermoelectric properties [9]. The GST system may also have a non-trivial band topology as found in, for example, superlattices of alternating Sb₂Te₃ and GeTe layers (GST-SL) [10]. Here, Sb₂Te₃ is a topological insulator (TI) [11,12] and GeTe is a normal insulator (NI) [13], which becomes superconducting below 1K [14–16]. The superlattice system consisting of L GST units, labeled as $[(\text{Sb}_2\text{Te}_3)_M(\text{GeTe})_N]_L$, is overall a topological or non-topological insulator depending on the relative layer thickness denoted by the indices M and N [7,17].

There are two mechanisms that contribute to the character of the band structure: (i) the physical intermixing of adjacent layers, and (ii) the coupling of topological modes [17,19] that appear at the interface of Sb₂Te₃ and GeTe (SG interface) in the superlattice. These two-dimensional modes are localized on the edge of (Sb₂Te₃) _{M} layer and have a linear Dirac dispersion with a helical spin structure. More strictly, the overall phase is governed by the competing hybridization of topological modes of the top and bottom edge of the (Sb₂Te₃) _{M} layer (intralayer coupling) and those of the neighboring layers through (GeTe) _{N} layer (interlayer coupling). To date, much of the investigation on GST as TI/NI multilayers, theoretical and experimental, focuses on monolayer/few monolayer superlattice units, e.g., $(M,N) = (1,2)$, or $(2,2)$ [7, 8, 10, 18, 20, 21]. GST structures in which the individual GeTe and Sb₂Te₃ are more bulk-like have received significantly less attention. In this context, a recent finding by some of the authors showed, unexpectedly, that in heterostructures of bulk-like Sb₂Te₃ and GeTe, the net number of topological modes is controlled by the GeTe layer even in a range where $M, N \gg 10$ [22]. In Ref. [22], the low-temperature magneto-transport of a Sb₂Te₃-GeTe-Sb₂Te₃ tri-layer structure was measured and the number of two-dimensional (2D) modes was inferred from the weak anti-localization characteristic [23–25]. Whereas one might expect that each TI/NI interface should host a topological mode, it was observed that for samples with a 15 nm-thick GeTe layer, the number of 2D modes was two fewer than expected. It was suggested that in a Sb₂Te₃-GeTe-Sb₂Te₃ (SGS) tri-layer, the topological modes flanking the GeTe layer hybridized even when separated by up to 15 nm and developed a gap of approximately 30 K. In order to understand this SGS tri-layer, i.e., TI/NI/TI tri-layer system, the role of band offsets at the SG interface, atomistic structure, and electronic structure of the junction have to be clarified.

In this paper, we find that the physical structure at the Sb₂Te₃-GeTe interface plays a crucial role in mediating interlayer interactions within the heterostructure. In particular, we find that under conditions of a sharp, well-defined interface, interactions between topological modes separated by more than a few nm is relatively weak. However, under more realistic conditions where the interface has some degree of intermixing, topological modes separated by as much as 10 nm couple and develop a gap of several meV. This strongly supports the findings of Nguyen *et al.* [22].

This paper is structured as follows: In Sec. 2, we present experimental measurements of the band offset between Sb₂Te₃ and GeTe on molecular-beam-epitaxy (MBE)-grown samples using X-ray photoemission spectroscopy (XPS). We then use first-principles calculations to obtain an independent estimate of the band offset at the SG interface using a range of experimentally relevant microstructures. Our estimates compare favorably with the XPS data, thereby validating the first-principles result. Moreover, the our experimental XPS indicates a significant intermixing between. Next, in Sec. 3, we develop a continuum model of an SGS tri-layer within a four-band framework, the parameters of which are obtained from our first-principles calculations. The continuum model can be used to study large systems that would be computationally too expensive to study directly using first-principles methods. Finally, in Sec. 4, we analyze the robustness of topological modes to chemical interactions and examine how the microscopic structure of the interfacial region may impact the interlayer coupling of topological modes.

2. BAND OFFSET

In this section, we discuss the band offset between the GeTe and Sb₂Te₃ layers in the GST heterostructure. First, in Sec. 2.1, we present experimental measurements of the band offset at the interface of GeTe and Sb₂Te₃ using XPS depth profiles. In Sec. 2.2, we then use first-principles calculations to evaluate the bulk crystal structure of GeTe and Sb₂Te₃, from which we obtain an independent evaluation of the band offset, which agrees with the experimental results. The agreement between experiment and theory validates the theoretical calculation, and provides a basis for the continuum model developed in Section 3 to describe larger systems.

2.1. EXPERIMENTAL EVALUATION

We use XPS measurements to determine the band offset between bulk GeTe and bulk Sb₂Te₃. Following Refs. [26–28], this is done by evaluating the difference of the core electron energy levels in bulk samples, and comparing this to the difference in the core energy levels in a heterostructure. Conventionally, this would require XPS spectra of three separate samples: a bulk GeTe film, a bulk Sb₂Te₃ film, and a heterostructure of the two in which the top layer is sufficiently thin (~ 5 nm) that the X-rays can penetrate it fully and sample both materials. However, such a procedure will have unknown systematic errors when considering Sb₂Te₃-GeTe heterostructures as the two compounds have a strong chemical affinity and will undergo significant intermixing, especially in the vicinity of the interface. Here, we obtain instead a “depth profile” of a single GeTe-Sb₂Te₃ heterostructure where XPS spectra are taken between successive Ar-ion etches of the sample, which successively remove the top layers of the heterostructure. The measurements are continued for the entire depth of the sample, i.e., until the Ar-ion etch fully depletes the material. This approach eliminates variations due to the different

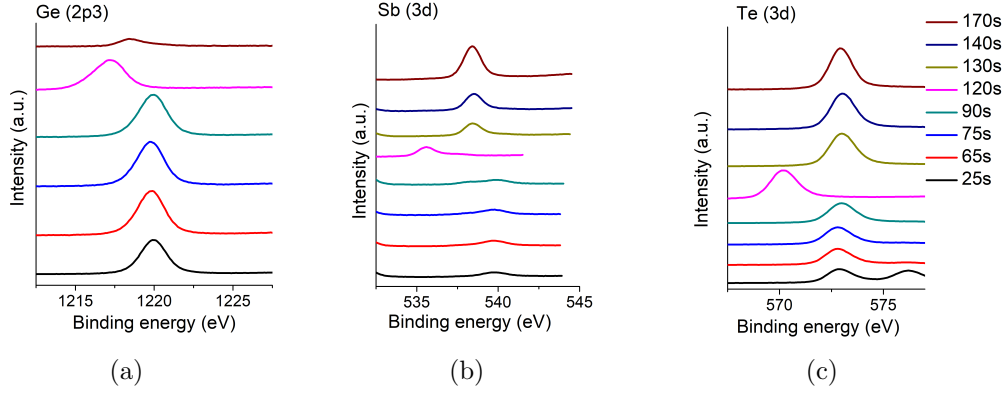


Figure 1. XPS spectra of the $\text{GeTe-Sb}_2\text{Te}_3$ heterostructure after consecutive ion milling steps for three different energy ranges near the (a) $\text{Ge}(2p_3)$, (b) $\text{Sb}(3d)$, and (c) $\text{Te}(3d)$ peaks. Spectra are obtained for eight different etch times of (bottom to top) $t = 25, 65, 75, 90, 120, 130, 140,$ and 170s , and we include an arbitrary offset between spectra to guide the eye. Panel (a) shows an initial pronounced $\text{Ge}(2p_3)$ peak at 1220eV that nearly vanishes after 170s of milling, indicating that the GeTe is fully eroded at that time. Consistent with this, panel (b) shows a clear peak at 540eV , corresponding to the $\text{Sb}(3d)$ transition, that emerges after 120s of etching, indicating the absence of Sb in the top layers of the original unetched sample. Panel (c) shows a consistent peak at 573eV corresponding to the $\text{Te}(3d)$ transition, indicating that the Te is present throughout the heterostructure. Panels (a) and (b) also show residual $\text{Sb}(\text{Ge})$ peaks in the $\text{Ge}(\text{Sb})$ -rich regions, which suggests an intermixing between the GeTe and Sb_2Te_3 layers.

growth conditions for separate samples. The samples considered here are MBE-grown heterostructures in which the GeTe (top) layer has a thickness of 11 nm and the Sb_2Te_3 layer is 25 nm thick. The samples are grown on a $\text{Si}(111)$ substrate as described in Ref. [22].

Figure 1 shows XPS depth profiles for different etching times $t = 25, 65, 75, 90, 120, 130, 140,$ and 170s in which the $\text{Ge}(2p_3)$ transition [Fig. 1(a)], the $\text{Sb}(3d)$ transition [Fig. 1(b)], and the $\text{Te}(3d)$ transition [Fig. 1(c)] is monitored. As expected, initially there is a pronounced Ge peak which begins to diminish at the same time the Sb peak appears, indicating that the top GeTe layer is completely eroded after 130s of etching. The $\text{Te}(3d)$ transition [Fig. 1(c)] shows little depth dependence, which is expected. The traces taken between 120s and 140s show features corresponding to both Ge and Sb , suggesting that the X-rays probe both layers in this range, which points to an intermixing between the layers. These traces also reflect the diffuse nature of interface between the two materials. The band offset ΔE_v is obtained as described in Refs. [26–28]:

$$\Delta E_v = (E_{\text{CL}}^{\text{Ge}} - E_v^{\text{Ge}}) - (E_{\text{CL}}^{\text{Sb}} - E_v^{\text{Sb}}) + \Delta E_{\text{CL}}. \quad (1)$$

Here, the first two terms on the right-hand side represent the difference in energy between the core level (CL) and valence band edge (E_v) of Ge and Sb , respectively. These are

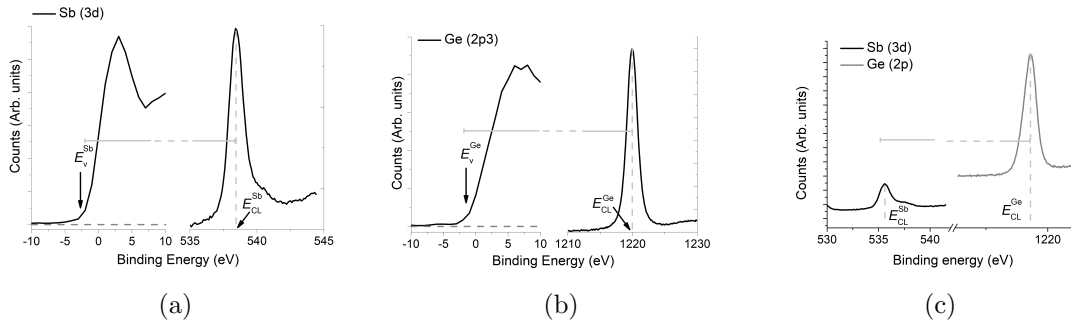


Figure 2. Absolute position of the (a) Sb(3d) and (b) Ge(2p3) core levels with respect to the valence band energy E_v . (a) shows an XPS spectrum measured in the Ge-rich phase and (b) shows an XPS spectrum in the Sb-rich phase. The valence band energy E_v is defined as the minimum energy at which emissions are observed, i.e., at which the XPS spectrum just becomes non-zero (indicated by arrows in (a) and (b)). This is obtained as the intersection of the binding energy curve with the background level in the respective left panels of Fig. 2(a) and 2(b). (c) XPS spectrum after 120 s of etching which contains signals from both Ge and Sb core levels, from which the difference in core energy levels is evaluated as shown.

Table 1. Fermi energy, valence band maximum (VBM), and conduction band minimum (CBM). All quantities are given in eV. The last row denotes the indirect band gap.

	Sb_2Te_3 (Rh)	Sb_2Te_3 (Rk)	GeTe (dRk)	GeTe (Rk)
Fermi level	0.00	-0.08	-0.13	0.22
VBM	-0.02	-0.11	-0.36	0.13
CBM	0.08	-0.06	0.11	0.22
Band Gap	0.10	0.05	0.47	0.09

obtained from the bulk spectra as shown in Figs. 2(a) and 2(b). The third term is the difference in energy between the core levels of Ge and Sb obtained from the combined spectrum shown in Fig. 2(c). The result for the band offset is $\Delta E_v = 0.4 \pm 0.1$ eV.

Further evidence for intermixing region is obtained in Fig. 3 where we show atom probe tomography (APT) of a $\text{Sb}_2\text{Te}_3/\text{GeTe}/\text{Sb}_2\text{Te}_3$ sample. APT is based on the evaporation of atoms in the form of ions from a single tip-shaped sample by means of an electric field. During the analyses, ions are projected from the apex of the tip onto a position-sensitive single ion detector [?] by the electric field. On the basis of the measured positions and the time-of-flight between the tip apex and the detector surface a 3D reconstruction of the analyzed volume is created [?]. Further details of the ATP can be found in the Supplementary Material [29].

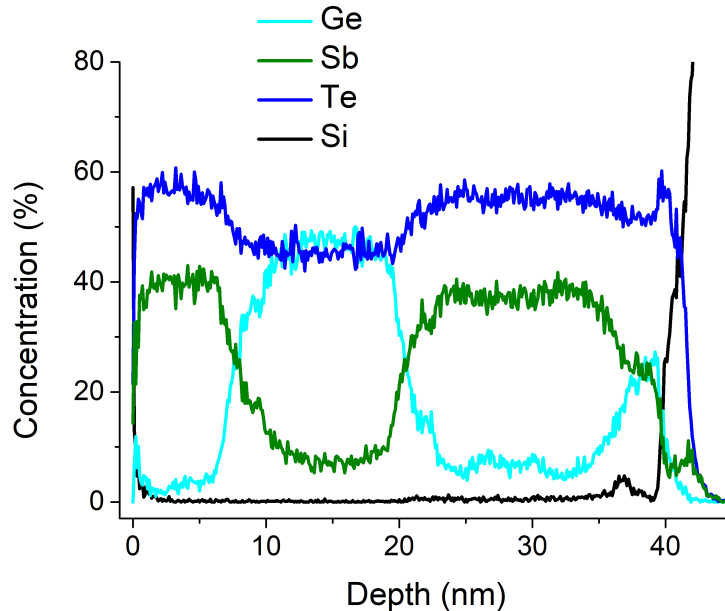


Figure 3. Atom probe tomography (APT) of $\text{Sb}_2\text{Te}_3/\text{GeTe}/\text{Sb}_2\text{Te}_3$ samples show a depth profile of the concentrations of Ge, Sb and Te through the sample thickness (see Supplementary Material for APT methods [29]). One clearly observes distinct Sb-rich, Ge-rich and Sb-rich regions separated by intermixed regions located at 8 nm and 22 nm. Within the Sb (Ge)-rich region there is a *relative concentration* of $< 20\%$ Ge (Sb) whereas in GST225 the relative concentrations of Ge and Sb are equal.

2.2. FIRST-PRINCIPLES CALCULATIONS

In this section, we present results for the band offset obtained from electronic structure calculations of bulk Sb_2Te_3 and GeTe via density functional theory (DFT). In our calculations, we use the SIESTA program package [30] and adopt the double zeta plus polarization function (DZP) level basis set. Our results are consistent with the experimental findings presented in the previous section. To evaluate the band offset and identify the SG interfacial electronic states, we make use of the non-equilibrium Greens function technique [31] combined with DFT (NEGF-DFT). Since NEGF-DFT satisfies semi-infinite boundary condition, our results are free from artificial size effects, which are often problematic in slab model calculations. NEGF-DFT calculations were carried out using the Smeagol program package [32,33]. We adopt an exchange correlation (XC) functional of the van der Waals (vW) correction, DF2 [34], for total energy calculations and use the local density approximation (LDA) to determine the band structure in NEGF-DFT calculations, where spin-orbit (SO) interaction are included.

At room temperature, bulk GeTe crystallizes in a disordered rock salt (dRk) structure and Sb_2Te_3 crystallizes in a rhombohedral layered (Rh) structure [35]. Hence, the conventional hexagonal cell can be taken as the unit cell for both, where the (111) direction of the rock salt corresponds to the (0001) in the conventional hexagonal cell. We set the c -axis to the (0001) direction and define the z -coordinate along the c -axis.

The SG interface plane is then perpendicular to the (0001) direction. In the conventional hexagonal cell, both GeTe (dRk) and Sb₂Te₃ (Rh) have a CBA/CBA/CBA/... stacking, where A, B, and C represent monolayers of Sb₂Te₃ or GeTe. In other words, the bulk unit cell of Sb₂Te₃ and GeTe consists of three monolayers, which may be denoted as (Sb₂Te₃)₃ and (GeTe)₃, respectively [35, 36]. The experimental values of the lattice constants are $a_0 = b_0 = 4.26 \text{ \AA}$ and $c_0 = 30.75 \text{ \AA}$ for Sb₂Te₃ (Rh) and $a_0 = b_0 = 4.17 \text{ \AA}$ and $c_0 = 10.90 \text{ \AA}$ for GeTe (dRk) [36]. Thus, there is a very small lattice mismatch at the SG interface. For simplicity, we fix the lattice constant as $a_0 = b_0 = 4.25 \text{ \AA}$ for both of Sb₂Te₃ and GeTe (as well as the SGS tri-layer) in our computational models and then allow all atoms in the cell to relax to their atomic positions. The atomic structures are shown in Figs. 4(a) and 4(b), respectively.

The band offset is calculated as follows: first, the Fermi level E_F is obtained from DFT calculations of bulk systems that include spin-orbit interactions. Then, we define an extended cell C by taking $1 \times 1 \times 3$ unit cells and apply the self-consistent NEGF-DFT. The left and right sides of C are connected to the bulk semi-infinitely by the self-energy terms, such that our calculations give the Greens function projected on C. Using the resulting Greens functions, we analyze the spectral density and evaluate the conduction band minima (CBM) and valence band maxima (VBM). Next, we carried out NEGF-DFT for the same C while the right side of the cell C is now terminated by vacuum. Practically, we took a vacuum region of $z_{\text{vac}} = 15.0 \text{ \AA}$ in the z -direction. Now, we can introduce the unique definition of the Fermi level E_F^0 using the vacuum level, i.e.,

$$E_F^0 = E_F - V_H(z = z_{\text{vac}}), \quad (2)$$

where V_H is the Hartree potential averaged over the xy plane. As the last step, we corrected the values of VBM and CBM by Eq. (2), which are denoted as E_v^0 and E_c^0 , respectively. We applied the above procedures to Sb₂Te₃ (Rh) and GeTe (dRk), and as a reference, also to the rock salt (Rk) structures of Sb₂Te₃ and GeTe which are possible crystal phases representing vacancy states or at high temperature [37–39]. The value of E_F^0 of Sb₂Te₃ (Rh) is -4.61 eV .

In Table 1, we set E_F^0 of Sb₂Te₃ (Rh) to zero and list the values of the VBM, the CMB and the Fermi level of different structures relative to this. The band offset between Sb₂Te₃ (Rh) and GeTe (dRk), given by the difference between the respective VBM is $\Delta E_v \approx 0.36 \text{ eV}$, which agrees well with our experimental value reported in Sec. 2. The validity of the calculations is also confirmed by noting that the calculated band gap of Sb₂Te₃ is 0.1 eV , which is consistent with its narrow gap, p -type semiconductor character. Likewise, the calculated band gap of GeTe (dRk) = 0.47 eV is close to the experimental value of 0.6 eV [13]. We note here that the band gap of GeTe (Rk) is underestimated by our theoretical calculation, but disorder is known to increase the experimental band gap, which is consistent with our results [35].

The present results suggest the validity of our computational model in order to analyze the topological modes of an SGS tri-layer quantitatively. In the next section, in

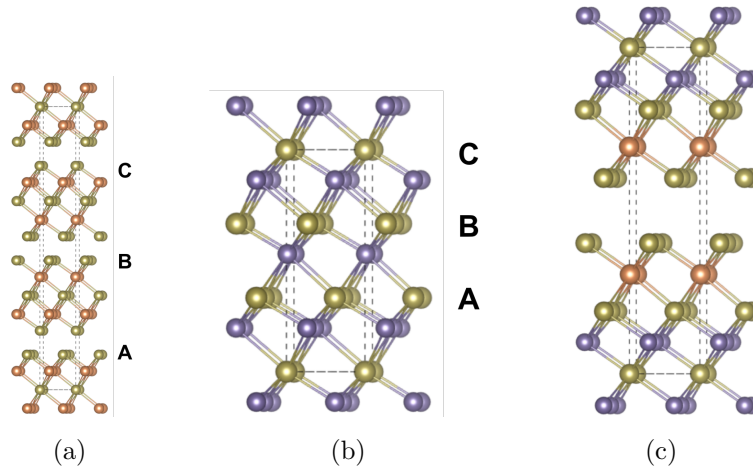


Figure 4. Crystal structures of bulk (a) Sb_2Te_3 (rhombohedral), (b) GeTe (disordered rock salt), and (c) GST_{225} (Kooi structure). The purple, dark yellow and orange balls represent Ge, Te, and Sb atoms, respectively. All structures are represented in the conventional hexagonal cell, which is indicated by dotted lines. The unit cells of Sb_2Te_3 and GeTe consist of three stacked monolayers of Sb_2Te_3 and GeTe , which are labeled by A, B, and C, respectively.

order to treat large heterostructures beyond the range of numerical DFT simulations, we construct an effective four-band model with parameters derived from our first-principles calculations.

3. FOUR-BAND CONTINUUM MODEL

In the previous section, we have both experimentally and theoretically elucidated the structure of the SG interface. Experimental measurements of the band gap obtained using XPS were shown to be consistent with theoretical results from *ab-initio* DFT calculations of a semi-infinite slab structure, which indicates that our computational DFT model is predictive for these systems. The aim of this section is to extend the theoretical model to tri-layer structures and to address the recent experiments by Nguyen *et al.* [22] by considering the qualitative effect of a thick, bulk-like GeTe intermediate layer on the embedded interface states.

While the numerical DFT method is in principle exact, i.e., it will accurately describe the inter- and intralayer coupling as well as the chemical intermixing at the interfaces, modeling very thick bulk-like heterostructures comes with a prohibitive numerical cost. In practice, we are restricted to very thin structures of typically less than ten layers. In order to make contact with the experiments on bulk-like structures of Ref. [22], in this section, we introduce an effective four-band model using parameter values derived from the bulk calculations presented in the previous section. This model allows us to describe tri-layer structures of arbitrary thickness. Indeed, as a main result of this paper, our findings indicate a significant interlayer-coupling of surface states

Table 2. Band parameters of the four-band continuum model. The parameter definitions are given in Eq. (3). Values for Sb₂Te₃ are taken from Ref. [12], parameters for GeTe and GST225 are extracted from a fit to our first-principles results. The Fermi level of Sb₂Te₃ is set to zero.

	A_0	A_2	B_0	B_2	C_0	C_1	C_2	M_0	M_1	M_2
Sb ₂ Te ₃	3.40	0.00	0.84	0.00	0.00	-12.39	-10.78	-0.22	19.64	48.51
GeTe	5.51	0.00	2.75	0.00	-0.13	-3.56	12.41	0.79	-25.17	-120.40
GST225	0.02	0.00	0.00	0.00	0.04	-6.99	2.21	0.14	16.74	14.82

across the GeTe layer, which is consistent with the experiment [22].

An effective four-band model is predictive for inter- and intralayer coupling effects, but it neglects the physical intermixing of the GeTe and Sb₂Te₃ phases at the interface, i.e., a reconfiguration of atomic positions. In order to take this into account, we consider additionally a model in which the GeTe film is replaced by a Ge₂Sb₂Te₅ (GST225) crystal phase, which is one of the most standard compositions of the GST alloy. We adopt the Kooi structure of GST225 [40], the crystal structure of which is shown in Fig. 4(c). To further support our effective model, in Sec. 4, we present ab-initio results for thin heterostructures that are consistent with the results obtained by the four-band model.

3.1. CONTINUUM MODEL OF HETEROSTRUCTURE

Topological insulators in the Bi₂Se₃ and Sb₂Te₃ family are often described by a four-band model Hamiltonian that captures the band structure near the Γ point. The model was first derived by Zhang *et al.* [12] and by Liu *et al.* [41]. The effective four-band Hamiltonian is

$$H = \begin{pmatrix} \varepsilon(\mathbf{k}) + M(\mathbf{k}) & B(k_z)k_z & 0 & A(k_{\parallel})k_{-} \\ B(k_z)k_z & \varepsilon(\mathbf{k}) - M(\mathbf{k}) & A(k_{\parallel})k_{-} & 0 \\ 0 & A(k_{\parallel})k_{+} & \varepsilon(\mathbf{k}) + M(\mathbf{k}) & -B(k_z)k_z \\ A(k_{\parallel})k_{+} & 0 & -B(k_z)k_z & \varepsilon(\mathbf{k}) - M(\mathbf{k}) \end{pmatrix}, \quad (3)$$

where, adopting the notation of Ref. [41], $\varepsilon(\mathbf{k}) = C_0 + C_1k_z^2 + C_2k_{\parallel}^2$, $M(\mathbf{k}) = M_0 + M_1k_z^2 + M_2k_{\parallel}^2$, $A(k_{\parallel}) = A_0 + A_2k_{\parallel}^2$, $B(k_z) = B_0 + B_2k_z^2$, $k_{\parallel}^2 = k_x^2 + k_y^2$, and $k_{\pm} = k_x \pm ik_y$. Here, the interface is aligned in the xy -plane, and the z -direction is perpendicular to the interface.

The parameters of Sb₂Te₃ were derived in Ref. [12] and are summarized in Tab. 2, where we define the zero of the energy scale at the Fermi level of Sb₂Te₃. Note that the parameters A_2 and B_2 , which relate to higher-order terms in k , are set to zero since we only consider the region close to Γ point. For calculations of multilayer structures, we also require parameter values for an effective model of the GeTe phase. Due to band inversion, the band gap of GeTe (dRk) increases at the L point in the rock salt structure [10, 42]. The four-band model (3) is still applicable, where the L point of the rock salt cell relates to the Γ point in the conventional hexagonal cell. We construct an effective Hamiltonian of GeTe (dRk) by fitting the first-principles data of the bulk unit

cell presented in Sec. 2.2 near the Γ point to our effective model. The parameter set is given in Tab. 2. Related parameters for a Hamiltonian that describes the GST225 (Kooi) phase are also given in Tab. 2.

For a slab geometry with an interface in the xy -plane, we loose translational invariance in the z direction. The Hamiltonian of a heterostructure takes the form (3) with z -dependent coefficients $A_1(z), A_2(z), \dots$ etc:

$$\hat{H}(k_x, k_y, k_z) \rightarrow \hat{H}(k_x, k_y, -i\partial_z). \quad (4)$$

Note that in the heterostructure, the second z -derivative must be written in a manifestly symmetric form to ensure a hermitian Hamiltonian, i.e., we replace [43]

$$-B_2 k_z^2 \rightarrow \frac{d}{dz} B_2(z) \frac{d}{dz}. \quad (5)$$

Eigenstates that solve $\hat{H}\Psi(z) = E\Psi(z)$ depend on the parallel momentum k_{\parallel} as well as the z coordinate. We consider solutions within a layer with the ansatz [43]

$$\Psi_{\alpha\beta}(z, E) = \Psi_{\alpha\beta}(E) e^{\beta\lambda_{\alpha}(E)z}, \quad (6)$$

where λ_{α} is a complex-valued function of E and $\alpha, \beta = \pm$. The eigenstate equation for $\Psi(z, E)$ reads

$$\begin{pmatrix} -\lambda_{\alpha}^2 D_- + L_1 & -i(\beta\lambda_{\alpha})B_0 & 0 & A_0 k_- \\ -i(\beta\lambda_{\alpha})B_0 & -\lambda_{\alpha}^2 D_+ + L_2 & A_0 k_- & 0 \\ 0 & A_0 k_+ & -\lambda_{\alpha}^2 D_- + L_1 & i(\beta\lambda_{\alpha})B_0 \\ A_0 k_+ & 0 & i(\beta\lambda_{\alpha})B_0 & -\lambda_{\alpha}^2 D_+ + L_2 \end{pmatrix} \Psi_{\alpha\beta}(E) = E\Psi_{\alpha\beta}(E) \quad (7)$$

with

$$\begin{aligned} D_{\pm} &= C_1 \mp M_1 \\ L_1 &= C_0 + M_0 + (C_2 + M_2)k_{\parallel}^2 \\ L_2 &= C_0 - M_0 + (C_2 - M_2)k_{\parallel}^2. \end{aligned} \quad (8)$$

The value of λ_{α} is be obtained in closed analytical form by solving Eq. (5), which gives [44, 45]

$$\lambda_{\alpha}^2(E) = -\frac{F}{2D_+D_-} + \alpha \frac{\sqrt{R}}{2D_+D_-}, \quad (9)$$

where

$$\begin{aligned} F &= B_0^2 + D_+(E - L_1) + D_-(E - L_2) \\ R &= F^2 - 4D_+D_-[(E - L_1)(E - L_2) - A_0^2 k_+ k_-]. \end{aligned} \quad (10)$$

For each value of $\beta\lambda_{\alpha}(E)$, there are two linearly independent eigenvectors:

$$\Psi_{\alpha\beta 1}(E) = \begin{pmatrix} E + \lambda_{\alpha}^2 D_+ - L_2 \\ -i(\beta\lambda_{\alpha})B_0 \\ 0 \\ A_0 k_+ \end{pmatrix}, \quad \Psi_{\alpha\beta 2}(E) = \begin{pmatrix} A_0 k_- \\ 0 \\ i(\beta\lambda_{\alpha})B_0 \\ E + \lambda_{\alpha}^2 D_- - L_1 \end{pmatrix}. \quad (11)$$

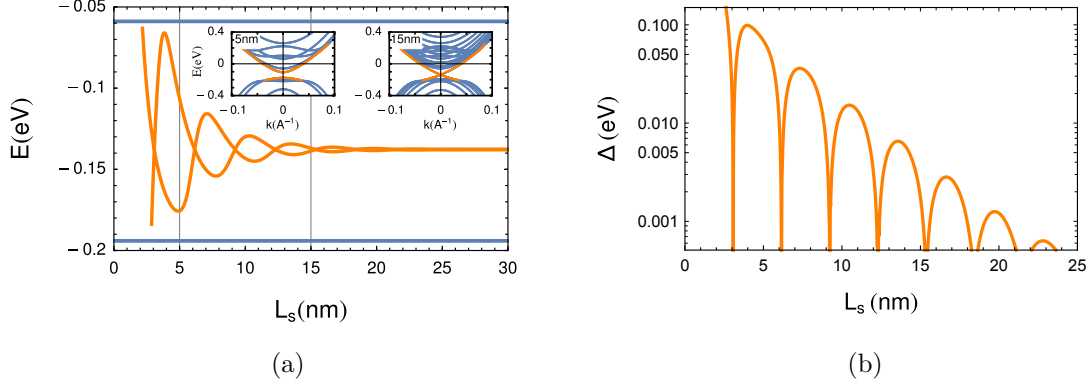


Figure 5. Band structure of a single Sb_2Te_3 slab as obtained from the four-band model. (a) Energy levels of the surface states at the Γ point as a function of slab thickness L_s . (b) Difference of the two surface states energies at the Γ point in the bulk band gap. When the slab thickness is larger than 15 nm, the two surface states are almost degenerate.

The full solution in each layer is composed of these eight eigenvectors. Eight boundary conditions then determine the relative magnitude of the eigenvectors (with the overall magnitude fixed by the normalization) and the energy E . The condition on E follows from the determinant of the boundary conditions.

It remains to determine boundary conditions. First, we require $\Psi = 0$ at the two boundaries of the slab (eight boundary conditions). Second, at each interface, we impose the continuity of the wavefunction and the current (which gives four boundary conditions per interface). This can be written as

$$\begin{aligned} \Psi(-\varepsilon) &= \Psi(+\varepsilon) \\ \mathcal{M}\Psi(-\varepsilon) &= \mathcal{M}\Psi(+\varepsilon), \end{aligned} \quad (12)$$

where the flux operator \mathcal{M} is obtained by integrating the Hamiltonian across the interface

$$\mathcal{M} = \begin{pmatrix} (C_1 + M_1) \frac{\partial}{\partial z} & iB_0 & 0 & 0 \\ iB_0 & (C_1 - M_1) \frac{\partial}{\partial z} & 0 & 0 \\ 0 & 0 & (C_1 + M_1) \frac{\partial}{\partial z} & -iB_0 \\ 0 & 0 & -iB_0 & (C_1 - M_1) \frac{\partial}{\partial z} \end{pmatrix}. \quad (13)$$

3.2. FOUR-BAND PARAMETERS AND APPLICATION TO SGS TRI-LAYER

Before presenting results for the SGS tri-layer structure, we consider a single Sb_2Te_3 (Rh) film to estimate the strength of the interlayer coupling. The single slab geometry has been solved in Refs. [44–46]. Results of this calculation using Sb_2Te_3 parameters are shown in Fig. 5. Figure 5(a) shows the position of the valence band maximum and the conduction band minimum at the Γ point as a function of the slab thickness L_s (orange lines). These states are surface states that are localized at the edge of the slab and gap

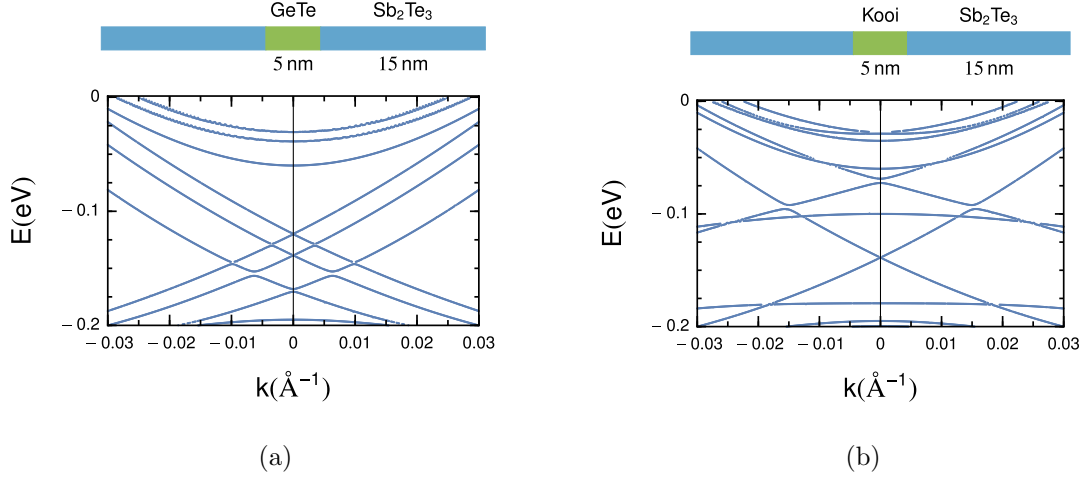


Figure 6. Calculated results for the band structure of an SGS tri-layer in the continuum model. (a) Band structure of an $\text{Sb}_2\text{Te}_3/\text{GeTe}/\text{Sb}_2\text{Te}_3$ tri-layer. (b) Band structure of an $\text{Sb}_2\text{Te}_3/\text{GST225}/\text{Sb}_2\text{Te}_3$ tri-layer.

out due to the intralayer coupling between the surface modes. The plot also includes the first bulk bands as blue lines. As for Bi_2Se_3 , there is an oscillating exponential decay of the gap with increasing slab thickness L_s . The inset illustrated the band structure near the Γ point for two values of the thickness $L_s = 5$ nm and 10 nm, where the massive gapped surface Dirac states is indicated by the orange lines and bulk bands by blue lines. Figure 5(b) shows the gap as a function of slab thickness L_s . As is apparent from the figure, surface states on the left and right edges are sufficiently decoupled for $L_s = 15$ nm, at which point the energy gap caused by intralayer coupling between the surface states is negligible (less than 0.01 eV). Furthermore, as is apparent from Fig. 5(a), the upper and lower energies of the surface states at Γ point are converged to 0.14 eV below the Fermi level of Sb_2Te_3 . The Sb_2Te_3 film is “bulk-like” when its thickness is larger than 15 nm.

We now discuss the band structure of an SGS tri-layer structure that consist of two outer Sb_2Te_3 layers and an embedded GeTe middle layer. Figure 6(a) shows results for the band structure near the Γ point computed as discussed in the previous section, where we choose an outer bulk-like Sb_2Te_3 layer of thickness $L_s = 15$ nm, and an inner GeTe layer of thickness $L_g = 5$ nm. While the surface states at the outer edges of the tri-layer are still localized at the slab energy of -0.14 eV, the inner Dirac states are shifted in energy, but no band gap opens at the Γ point. Note that the numerical result is essentially unchanged for different values of the thickness L_g of the inner GeTe layer, and a gap opening at the Γ point is only observed for very small values $L_g < 2$ nm. This result suggests that (i) the interlayer coupling is completely suppressed even for moderate GeTe layers and (ii) that the perturbation of the GeTe wave function is sufficiently weak that the band structure of SG interfacial state is unchanged. This is a very reasonable result considering the large offset of the GeTe valence band maximum and conduction band

minimum compared to the Sb₂Te₃ layer: The VBM and CBM of Sb₂Te₃ are located within the band gap of GeTe and there are no GeTe states in the energy range of surface states. Interlayer coupling of topological mode is suppressed.

As an alternative model, we examine an SGS structure in which the GeTe layer is replaced by GST225 (Kooi), the thickness of which L_k is also fixed at 5 nm. The results are summarized in Fig. 6(b). Interestingly, and in contrast to the previous case, we find a band gap opening at the Γ point. The band gap appears to close at points away from the Γ point, but this closed gap should be considered as an accidental degeneracy of the wave functions originating from the band structure of Sb₂Te₃ and GST225(Kooi), rather than any topological modes.

4. FIRST-PRINCIPLES CALCULATIONS OF INTERFACIAL STATES IN SGS TRI-LAYER

The continuum model assumes that the Hamiltonian derived from the (homogeneous) bulk structure is applicable to the heterostructure junction. Although we mimicked the effect of physical intermixing of chemical species by introducing the GST225 layer, effects due to local electronic states and/or vacancies, which we refer to as “chemical interactions”, are not represented. While charge transfer or charge accumulation by impurities at the SG interface is expected to be sufficiently small (as the electron affinity of both Sb₂Te₃ and GeTe is strong), the robustness of any topological mode against local fields arising from chemical interactions effect is not clear. In order to address this, in the following, we extract interfacial states of various thin SGS tri-layers directly by using NEGF-DFT.

In our computational model of the tri-layer, the left- and right-hand side of Sb₂Te₃ is represented explicitly by $1 \times 1 \times 3$ unit cells, where the outermost cells are connected to the bulk by self-energy terms as discussed in Sec. 2.2. Hence, different from the previous section, we can only consider the embedded interfacial state on the SG interface sides to analyze the topological mode, i.e., the intralayer-coupling is automatically eliminated. We consider three separate models with three separate structures for the NI part:

$$\begin{aligned} \text{(Model A): } & [(\text{Sb}_2\text{Te}_3)_9] / (\text{GeTe})_{3n} / [(\text{Sb}_2\text{Te}_3)_9] \\ \text{(Model B): } & [(\text{Sb}_2\text{Te}_3)_9] / (\text{Ge}_2\text{Te}_2)(\text{GeTe})_{3(n-2)}(\text{Ge}_2\text{Te}_2) / [(\text{Sb}_2\text{Te}_3)_9] \\ \text{(Model C): } & [(\text{Sb}_2\text{Te}_3)_9] / (\text{GST225})_m (\text{GeTe})_{3(n-2)} (\text{GST225})_m [(\text{Sb}_2\text{Te}_3)_9] \end{aligned}$$

In our notation, $[(\text{Sb}_2\text{Te}_3)_3]_2$, for example, denotes a stacking of the two (conventional hexagonal) unit cells of the Sb₂Te₃ crystal, i.e., it is a stacking of six Sb₂Te₃ quintuple monolayers (QLs). The intermediate layer in model A is a GeTe (dRk) layer. Here, the stacked numbers of (GeTe)₃ units, n , is taken as $n = 6$ (recall that a stacking of three GeTe monolayers is also the unit cell of the GeTe (dRK) bulk crystal in the conventional hexagonal cell). A change in the interface structure is taken into account in model (B), which contains a vacancy layer at the boundary of a GeTe (dRk)

phase. Here, the label (Ge₂Te₂) represents a vacancy layer that consists of a single (GeTe)₃ block. Finally, in model (C) we introduce two unit cells of GST225 on either side of GeTe as an intermixing region, i.e., $m = 2$. The outermost regions are connected to bulk Sb₂Te₃ (Rh). The 2D band dispersion of the interface is extracted by projecting the density of states (DOS) on the interface, and is exactly calculated from the Greens function as a function of energy E and wave vector k_{\parallel} . We take k to point along M- Γ -K line and the DOS was projected on each QL in the junction. We present the projected band structure at three separate positions: (a) the Sb₂Te₃-QL closest to the SG interface plane, (b) the secondary neighboring QL, and (c) the third QL in order to analyze the localization of topological mode. We labeled the above the three QLs as QL⁽¹⁾, QL⁽²⁾, and QL⁽³⁾, respectively. In our notation, [(Sb₂Te₃)₃]₂, for example, denotes a stacking of the two (conventional hexagonal) unit cells of the Sb₂Te₃ crystal, i.e., it is a stacking of six Sb₂Te₃ quintuple monolayers (QLs). The intermediate layer in model A is a GeTe (dRk) layer. Here, the stacked numbers of (GeTe)₃ units, n , is taken as $n = 6$ (recall that a stacking of three GeTe monolayers is also the unit cell of the GeTe (dRK) bulk crystal in the conventional hexagonal cell). A change in the interface structure is taken into account in model (B), which contains a vacancy layer at the boundary of a GeTe (dRk) phase. Here, the label (Ge₂Te₂) represents a vacancy layer that consists of a single (GeTe)₃ block. Finally, in model (C) we introduce two unit cells of GST225 on either side of GeTe as an intermixing region, i.e., $m = 2$. The outermost regions are connected to bulk Sb₂Te₃ (Rh). The 2D band dispersion of the interface is extracted by projecting the density of states (DOS) on the interface, and is exactly calculated from the Greens function as a function of energy E and wave vector k_{\parallel} . We take k to point along M- Γ -K line and the DOS was projected on each QL in the junction. We present the projected band structure at three separate positions: (a) the Sb₂Te₃-QL closest to the SG interface plane, (b) the secondary neighboring QL, and (c) the third QL in order to analyze the localization of topological mode. We labeled the above the three QLs as QL⁽¹⁾, QL⁽²⁾, and QL⁽³⁾, respectively.

In models (A) and (B), the extracted 2D band structure on QL⁽³⁾ is very similar to that of bulk Sb₂Te₃ (Rh) as given in Fig. 6(a). Although a very weak spectral density coming from the DOS of QL⁽²⁾ is found, the electronic state in QL⁽³⁾ is essentially a bulk state. In contrast, the projected band dispersion of QL⁽¹⁾ is more complicated and shows strong hybridization with the states of GeTe, i.e., the Sb₂Te₃ layer immediately adjacent to GeTe is strongly perturbed by chemical interactions. In the QL⁽²⁾ of model (B), we find a clear Dirac cone similar to the clean Sb₂Te₃ surface state. However, for model (A), we observe a Rashba-type split band rather than topological mode. These results lead to the following conclusions: first, the interfacial state characterized as the surface state of Sb₂Te₃ can be localized narrowly in the secondary neighboring Sb₂Te₃ monolayer in the junction; and second, the topological mode is not robust to chemical interaction even when the band offset is sufficiently large. By comparing models (A) and (B), the existence of a vacancy layer at the SG interface induces a significant chemical interaction effect. The local electric field due to a (GeTe)₃ block in the SG interface

works as a built-in asymmetric external field and gives rise to a Rashba-type interfacial state even though the topological mode is protected by GeTe block containing a vacancy layer, i.e., Ge₂Te₂. Interestingly, in contrast to model (A) and model (B), we found that 2D band on QL⁽³⁾ of model (C) does not converge to that of bulk. The presence of GST225 opens large band gap and the band dispersion is more NI-like near the Γ point. This result is also found in the continuum model, and thus the interlayer coupling of the wave function across GST225 is more long-ranged than in the cases with GeTe or vacancy layer + GeTe.

Model (C) represents a somewhat more realistic intermixing at the SG interface than the continuum model, i.e, GST225 is only narrow sublayer of NI as (GST225)_m[(GeTe)₃]_(n-2)(GST225)_m, where $(m, n) = (2, 6)$. According to the results of model (A) and (B), the above GeTe block is sufficiently thick to suppress interlayer coupling of topological modes from the two Sb₂Te₃ slabs. In other words, the large band gap at Γ is a result of local interaction (and hybridization) of each topological mode and electronic state narrowly localized on GST225. However, if the intermixing region of GST225 is sufficiently thick in the normal insulator part, the topological modes can be made to couple by tuning “bulk-like” thickness of the NI in the SGS tri-layer. This offers a very plausible explanation for the results observed by Nguyen *et al.* [22] since, experimentally, we find clear evidence of an intermixing region even in bulk-like SGS heterostructures (Figs. 1 and 3).

5. CONCLUSIONS

In this paper, we have studied the band structure of bulk-like heterostructures of Sb₂Te₂ and GeTe as a prototypical TI-NI system. We have focused on the interfacial region between these materials and shed light on the conditions under which the topological mode may or may not be present. We have laid particular emphasis on understanding realistic structures in which the interface is not perfect, but rather contains an intermixed phase of the parent compounds Sb₂Te₃ and GeTe. Our principal finding is that the presence of this intermediate phase serves to enhance the length over which topological modes may interact with each other. Importantly, we confirm experimentally that SGS heterostructures show a degree of intermixing, thereby underlining the relevance of our findings to the existing experimental literature on SGS systems. Of particular importance in this context is the experimental work by Nguyen *et al.* [22] which observes unexpectedly long-ranged interactions between topological modes in an SGS heterostructure. Our findings provide a natural explanation for these results and lay the foundation for future work wherein superlattices of bulk-like Sb₂Te₃ and GeTe layers can be used to deterministically produce different topological phases [19].

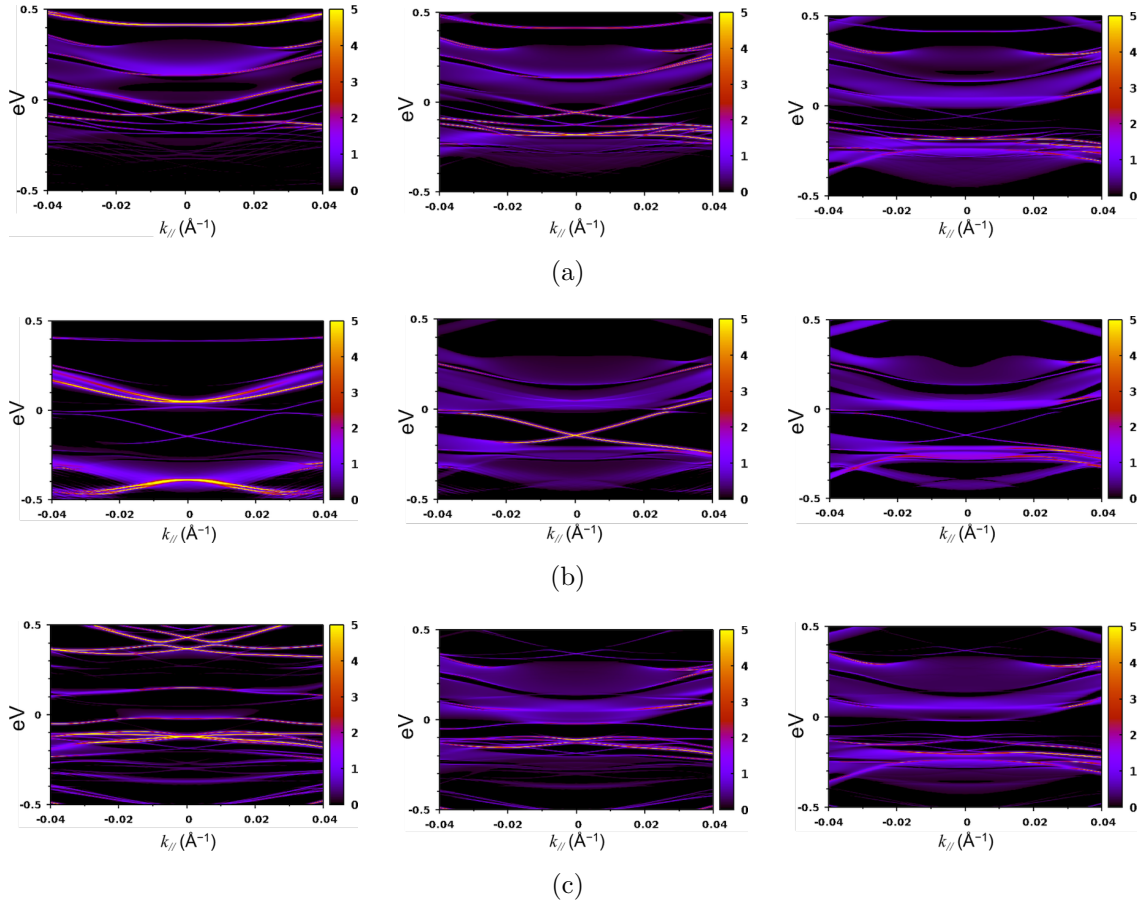


Figure 7. The extracted 2D band structures projected on a Sb_2Te_3 quintuple layer in the SGS tri-layer system by NEGF-DFT calculation. The Fermi level of bulk Sb_2Te_3 is set to zero. The zero of k_{\parallel} is at the Γ point, and k_{\parallel} is positive along the Γ -K line and negative along the Γ -M line. Three SGS tri-layer structures denoted as model A, B, and C were examined (see Sec. 4 of the text for the definition), corresponding to panels (a), (b), and (c), respectively. The left column is the 2D band structure projected on $\text{QL}^{(1)}$, i.e., the Sb_2Te_3 quintuple layer nearest to the GeTe (or GST225) block. The middle and right columns show band structures projected on the second ($\text{QL}^{(2)}$) and third ($\text{QL}^{(3)}$) nearest quintuple layer, respectively.

Acknowledgments

This work was supported by EPSRC, UK, CREST, JST (Grant No. JPMJCR14F1) and Peterhouse, Cambridge.

References

- [1] Raoux S, Xiong F, Wuttig M and Pop E 2014 *MRS Bulletin* **39** 703
- [2] Kato N, Fukano T, Takeda Y, Takeichi A, Motohiro T and Kawai S 2006 *Journal of Applied Physics* **100** 113115
- [3] Yamada N, Ohno E, Akahira N, Nishiuchi K, Nagata K and Takao M 1987 *Japanese Journal of Applied Physics* **26** 61

- [4] Simpson R E, Fons P, Kolobov A V, Fukaya T, Krbal M, Yagi T and Tominaga J 2011 *Nature Nanotechnology* **6** 501
- [5] Chen M, Rubin K A and Barton R W 1986 *Applied Physics Letters* **49** 502
- [6] Inoue N and Nakamura H 2019 *Faraday Discuss.* **213**(0) 303
- [7] Tominaga J, Kolobov A V, Fons P, Nakano T and Murakami S 2014 *Advanced Materials Interfaces* **1** 1300027
- [8] Tominaga J, Kolobov A V, Fons P J, Wang X, Saito Y, Nakano T, Hase M, Murakami S, Herfort J and Takagaki Y 2015 *Science and Technology of Advanced Materials* **16** 014402
- [9] Ibarra-Hernández W and Raty J Y 2018 *Phys. Rev. B* **97**(24) 245205
- [10] Sa B, Zhou J, Sun Z, Tominaga J and Ahuja R 2012 *Phys. Rev. Lett.* **109**(9) 096802
- [11] Hsieh D, Xia Y, Qian D, Wray L, Meier F, Dil J H, Osterwalder J, Patthey L, Fedorov A V, Lin H, Bansil A, Grauer D, Hor Y S, Cava R J and Hasan M Z 2009 *Phys. Rev. Lett.* **103**(14) 146401
- [12] Zhang H, Liu C X, Qi X L, Dai X, Fang Z and Zhang S C 2009 *Nature Physics* **5** 438
- [13] Tsu R, Howard W E and Esaki L 1968 *Phys. Rev.* **172**(3) 779
- [14] Hein R A, Gibson J W, Mazelsky R, Miller R C and Hulm J K 1964 *Phys. Rev. Lett.* **12**(12) 320
- [15] Narayan V, Nguyen T A, Mansell R, Ritchie D and Mussler G 2016 *physica status solidi (RRL) – Rapid Research Letters* **10** 253
- [16] Narayan V, Verpoort P C, Dann J R A, Backes D, Ford C J B, Lanius M, Jalil A R, Schüffelgen P, Mussler G, Conduit G J and Grützmacher D 2019 *Phys. Rev. B* **100**(2) 024504
- [17] Halász G B and Balents L 2012 *Phys. Rev. B* **85**(3) 035103
- [18] Nakamura H, Rungger I, Sanvito S, Inoue N, Tominaga J and Asai Y 2017 *Nanoscale* **9**(27) 9386
- [19] Burkov A A and Balents L 2011 *Phys. Rev. Lett.* **107**(12) 127205
- [20] Bang D, Awano H, Saito Y and Tominaga J 2016 *AIP Advances* **6** 055810
- [21] Qian H, Tong H, Zhou L J, Yan B H, Ji H K, Xue K H, Cheng X M and Miao X S 2016 *Journal of Physics D: Applied Physics* **49** 495302
- [22] Nguyen T A, Backes D, Singh A, Mansell R, Barnes C, Ritchie D A, Mussler G, Lanius M, Grützmacher D and Narayan V 2016 *Scientific Reports* **6** 27716
- [23] Hikami S, Larkin A I and Nagaoka Y 1980 *Progress of Theoretical Physics* **63** 707 ISSN 0033-068X
- [24] Backes D, Huang D, Mansell R, Lanius M, Kampmeier J, Ritchie D, Mussler G, Gumbs G, Grützmacher D and Narayan V 2017 *Phys. Rev. B* **96**(12) 125125
- [25] Backes D, Huang D, Mansell R, Lanius M, Kampmeier J, Ritchie D, Mussler G, Gumbs G, Grützmacher D and Narayan V 2019 *Phys. Rev. B* **99**(12) 125139
- [26] Kim J J, Kobayashi K, Ikenaga E, Kobata M, Ueda S, Matsunaga T, Kifune K, Kojima R and Yamada N 2007 *Phys. Rev. B* **76**(11) 115124
- [27] Kraut E A, Grant R W, Waldrop J R and Kowalczyk S P 1980 *Phys. Rev. Lett.* **44**(24) 1620
- [28] Fang L W W, Zhao R, Zhang Z, Pan J, Shi L, Chong T C and Yeo Y C 2011 *Applied Physics Letters* **98** 132103
- [29]
- [30] Soler J M, Artacho E, Gale J D, García A, Junquera J, Ordejón P and Sánchez-Portal D 2002 *Journal of Physics: Condensed Matter* **14** 2745
- [31] Datta S 1997 *Electronic Transport in Mesoscopic Systems* (Cambridge University Press)
- [32] Rocha A R, García-Suárez V M, Bailey S, Lambert C, Ferrer J and Sanvito S 2006 *Phys. Rev. B* **73**(8) 085414
- [33] Rungger I and Sanvito S 2008 *Phys. Rev. B* **78**(3) 035407
- [34] Klimeš J, Bowler D R and Michaelides A 2009 *Journal of Physics: Condensed Matter* **22** 022201
- [35] Da Silva J L F, Walsh A and Lee H 2008 *Phys. Rev. B* **78**(22) 224111
- [36] Nonaka T, Ohbayashi G, Toriumi Y, Mori Y and Hashimoto H 2000 *Thin Solid Films* **370** 258
- [37] Sun Z, Zhou J and Ahuja R 2006 *Phys. Rev. Lett.* **96**(5) 055507
- [38] Ohyanagi T, Kitamura M, Araidai M, Kato S, Takaura N and Shiraiishi K 2014 *Applied Physics Letters* **104** 252106
- [39] Di Sante D, Barone P, Bertacco R and Picozzi S 2013 *Advanced Materials* **25** 509

- [40] Kooi B J and De Hosson J T M 2002 *Journal of Applied Physics* **92** 3584
- [41] Liu C X, Qi X L, Zhang H, Dai X, Fang Z and Zhang S C 2010 *Phys. Rev. B* **82**(4) 045122
- [42] Liebmann M, Rinaldi C, Di Sante D, Kellner J, Pauly C, Wang R N, Boschker J E, Giussani A, Bertoli S, Cantoni M, Baldrati L, Asa M, Vobornik I, Panaccione G, Marchenko D, Sánchez-Barriga J, Rader O, Calarco R, Picozzi S, Bertacco R and Morgenstern M 2016 *Advanced Materials* **28** 560
- [43] Bastard G and Brum J 1986 *IEEE Journal of Quantum Electronics* **22** 1625 ISSN 1558
- [44] Zhou B, Lu H Z, Chu R L, Shen S Q and Niu Q 2008 *Phys. Rev. Lett.* **101**(24) 246807
- [45] Shan W Y, Lu H Z and Shen S Q 2010 *New Journal of Physics* **12** 043048
- [46] Linder J, Yokoyama T and Sudbø A 2009 *Phys. Rev. B* **80**(20) 205401